LRP 571/97 April 1997

EFFECT OF PLASMA SHAPE ON CONFINEMENT AND MHD BEHAVIOUR IN THE TCV TOKAMAK

H. Weisen, J.-M. Moret, S. Franke, I. Furno,
Y. Martin, M. Anton, R. Behn, M. Dutch,
B.P. Duval, F. Hofmann, B. Joye, C. Nieswand,
Z.A. Pietrzyk, W. Van Toledo

submitted for publication to
Nuclear Fusion

Effect of Plasma Shape on Confinement and MHD Behaviour in the TCV Tokamak

H. Weisen, J.-M. Moret, S. Franke, I. Furno, Y. Martin, M. Anton[†], R. Behn, M. Dutch, B.P. Duval, F. Hofmann, B. Joye, C. Nieswand, Z.A. Pietrzyk, W. van Toledo

Centre de Recherches en Physique des Plasmas
Association EURATOM - Confédération Suisse
École Polytechnique Fédérale de Lausanne
CH-1015 Lausanne, Switzerland

[†]present address: Max Planck Institut für Plasmaphysik, D-857480 Garching, Germany

Abstract. The energy confinement time of TCV ohmic L-mode discharges depends strongly on plasma shape. For fixed average current and electron densities, confinement times increase with plasma elongation and decrease with (positive) plasma triangularity. This dependence can be explained by the geometrical effects of flux surface expansion and compression on the temperature gradients together with the effect of power degradation, without a need to invoke a shape dependence of the transport coefficients. A global factor of merit, the shape enhancement factor H_S is introduced to quantify this geometrical effect. The shape enhancement factor also has the potential to improve the description of the shape dependence in existing inter-device scaling laws. Modified versions of Neo-Alcator scaling and of Rebut-Lallia-Watkins scaling provide successful descriptions of ohmic L-mode confinement for a large variety of plasma shapes in TCV by making use of H_S. MHD activity is also strongly dependent on plasma shape. Sawtooth amplitudes are largest at positive triangularity and sometimes vanish at negative triangularity, where the amplitude of MHD modes is highest. We show that the changes in MHD behaviour are to a large extent consequences of the confinement changes produced in these shaping experiments.

1.0 Experimental conditions

The distinctive feature of TCV (Tokamak à Configuration Variable) is a vacuum vessel with a height-to-width ration of 3 surrounded by 16 poloidal field shaping coils. This construction permits the creation of highly elongated and strongly shaped plasmas [Hofmann et al, 1994, 1995]. The machine therefore offers a unique capability to extend the world confinement database and to improve our understanding of transport in shaped plasmas. Basic parameters in the experiments reported are R_0=0.88 m, a=0.25m for the major and minor radius and B_T=1.43T for the toroidal magnetic field.

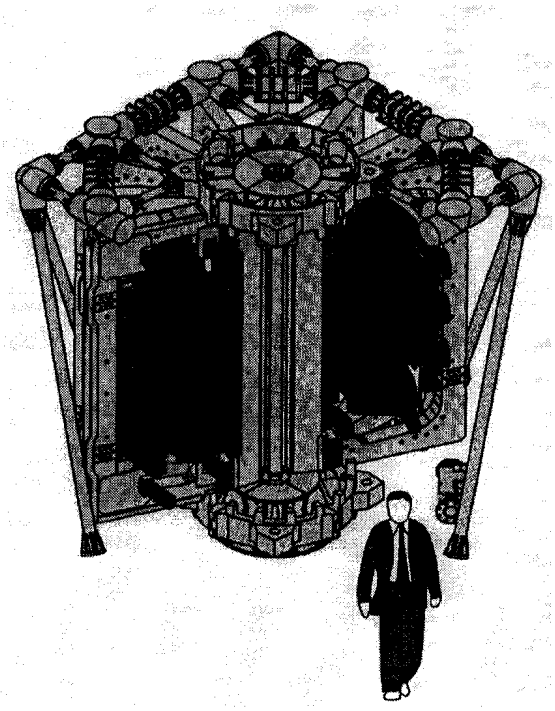

Fig. 1 The TCV device

In the work presented the influence of plasma shape on the energy confinement and MHD behaviour has been investigated by way of a large variation of the plasma shape, from circular to highly elongated equilibria and from strongly D-shaped (positive triangularity) to inverse D-shaped equilibria (negative triangularity). The discharges investigated consist of 230 limited ohmic L-mode discharges in which elongation κ_a, triangularity δ_a, edge safety factor q_a at the last closed flux surface and line average density $\bar{n}_e$ were systematically scanned in the range $1.06 < \kappa_a < 1.86$, $-0.41 < \delta_a < 0.72$, $2.3 < q_a < 6$, $2.85\times10^{19}m^{-3} < \bar{n}_e < 8.5\times10^{19}m^{-3}$.

The TCV shape control system was programmed to produce equilibria such that the shape of the last closed flux surface is defined by the analytical contour, $R = R_0 + a\cos(\theta + \delta_a \sin\theta)$, and $Z = a\kappa_a \sin\theta$. A current scan has been performed in each configuration in order to encompass a variation in q_a from 2.3 to 6, corresponding to plasma currents ranging from 105kA to 565kA. These current scans are necessary to separate any influence of the shape on the confinement from an intrinsic dependence on the plasma current. The line average density, $\bar{n}_e$, has also been varied to elucidate any confinement dependence on the density. Most of the data are in the linear ohmic confinement regime where total confinement time scales with density. All data are obtained in stationary conditions, established for at least 0.5s, with the plasma limited by the graphite tiled central column and D_2 as the filling gas.

1.1 Energy confinement

The confinement properties of these plasmas are quantified by the electron energy confinement time, $\tau_{Ee} = W_e/P_{oh}$, where P_{oh} is the ohmic input power. The total electron energy, W_e, is obtained by volume integration of Thomson scattering measurements at 10 spatial positions. For a given plasma shape, τ_{Ee} follows the usual ohmic behaviour, increasing with q_a and density. Most of the discharges in this study were restricted to values of $\bar{n}_e$ below which τ_{Ee} saturates on TCV. In all conditions a strong dependence of τ_{Ee} on the plasma shape is observed: for fixed q_a, a slight improvement with elongation and a marked reduction with positive triangularity. For the range of triangularity studied, the relative variation in τ_{Ee} is typically 2 and reaches 3 at the highest density. This shape dependence is presented in figure 2 for 2 ranges of safety factor and three ranges of electron density. Note that it was not possible in these experiments to produce highly elongated plasmas with high density and negative triangularity because of the appearance of large MHD modes and locked mode disruptions.

1.2 Sawtooth behaviour and MHD mode activity

The amplitude of sawtooth crashes (internal disruptions) varies strongly with triangularity, being largest at positive triangularity and sometimes vanishing at negative triangularity, as seen in figure 3. The figure shows the relative crash amplitude obtained from an X-ray emission measurement using a photodiode viewing the plasma core through a 50 μm thick beryllium foil.

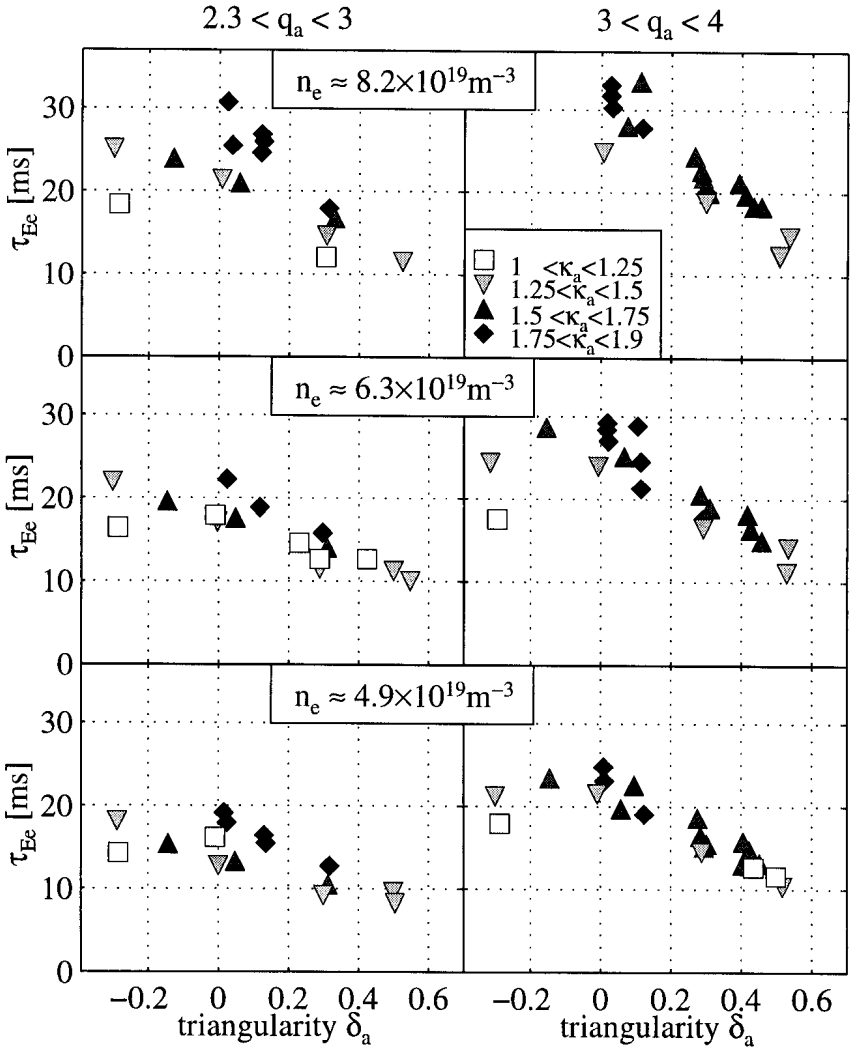

Fig. 2 Shape dependence of the electron energy confinement time for three ranges of line averaged electron density and two ranges of edge safety factor. Symbols represent classes of elongation: squares 1<κ_α<1.25; down triangles 1.25 <κ_α< 1.75; up triangles 1.5 <κ_α<1.75; diamonds 1.75 <κ_α< 2.

The gross amplitude $\Delta E_x/E_x$, where E_x is the measured emission is corrected for the temperature dependence of the X-ray emissivity of the dominant impurity, carbon, using the factor $\gamma_x = d(\ln E_x)/d(\ln T_e(0))$. This correction factor decreases from 2 to 1 over the range of central temperatures in the dataset (400-1100 eV). As a result the amplitudes shown in figure provide an estimate of the relative core pressure variation caused by the sawtooth crash.

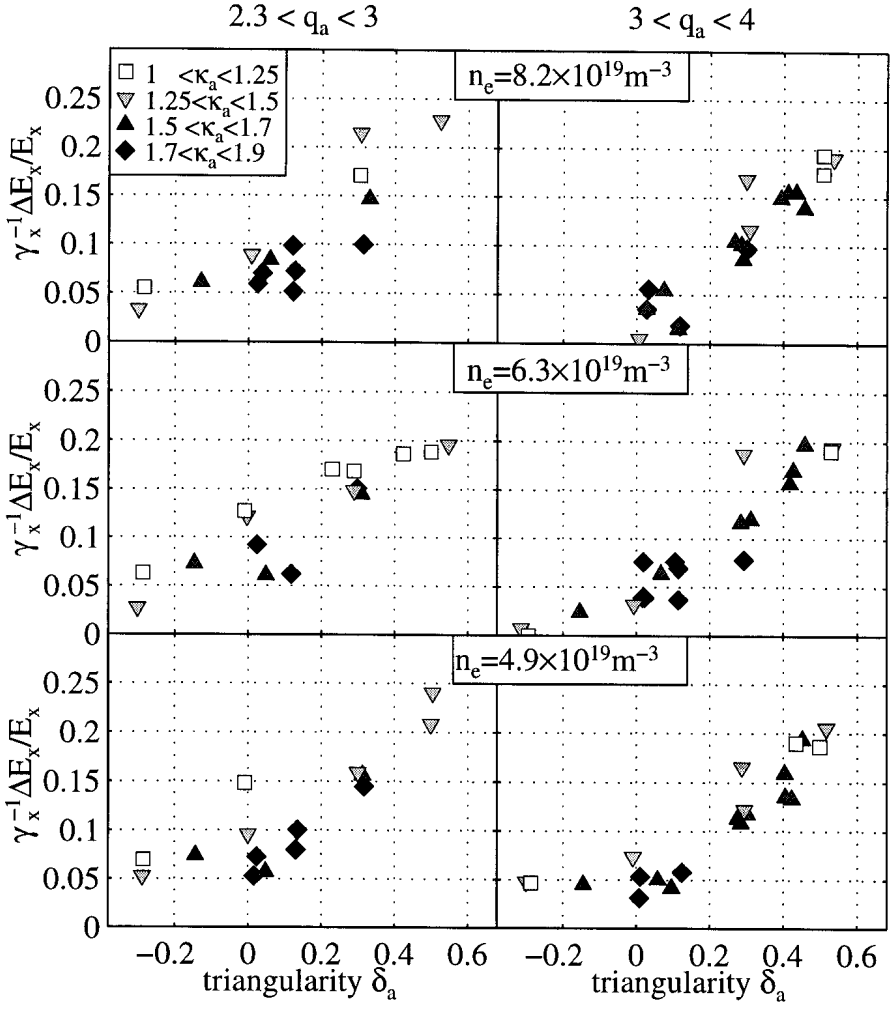

Fig. 3 Shape dependence of sawtooth amplitudes. Symbols as figure 2.

Figure 4 shows the raw X-ray emission measurement (top) and sawtooth inversion contours together with the contour of the last closed flux surface (LCFS, bottom) for four discharges with different triangularities. The inversion contours were determined from a sequence of soft X-ray tomographic inversions, using biorthogonal decomposition to extract inversion radii and mode structures [Anton et al 1996, Furno et al 1997]. The figure shows that as sawtooth amplitudes decrease at low and negative triangularity, the amplitude of MHD modes increases.

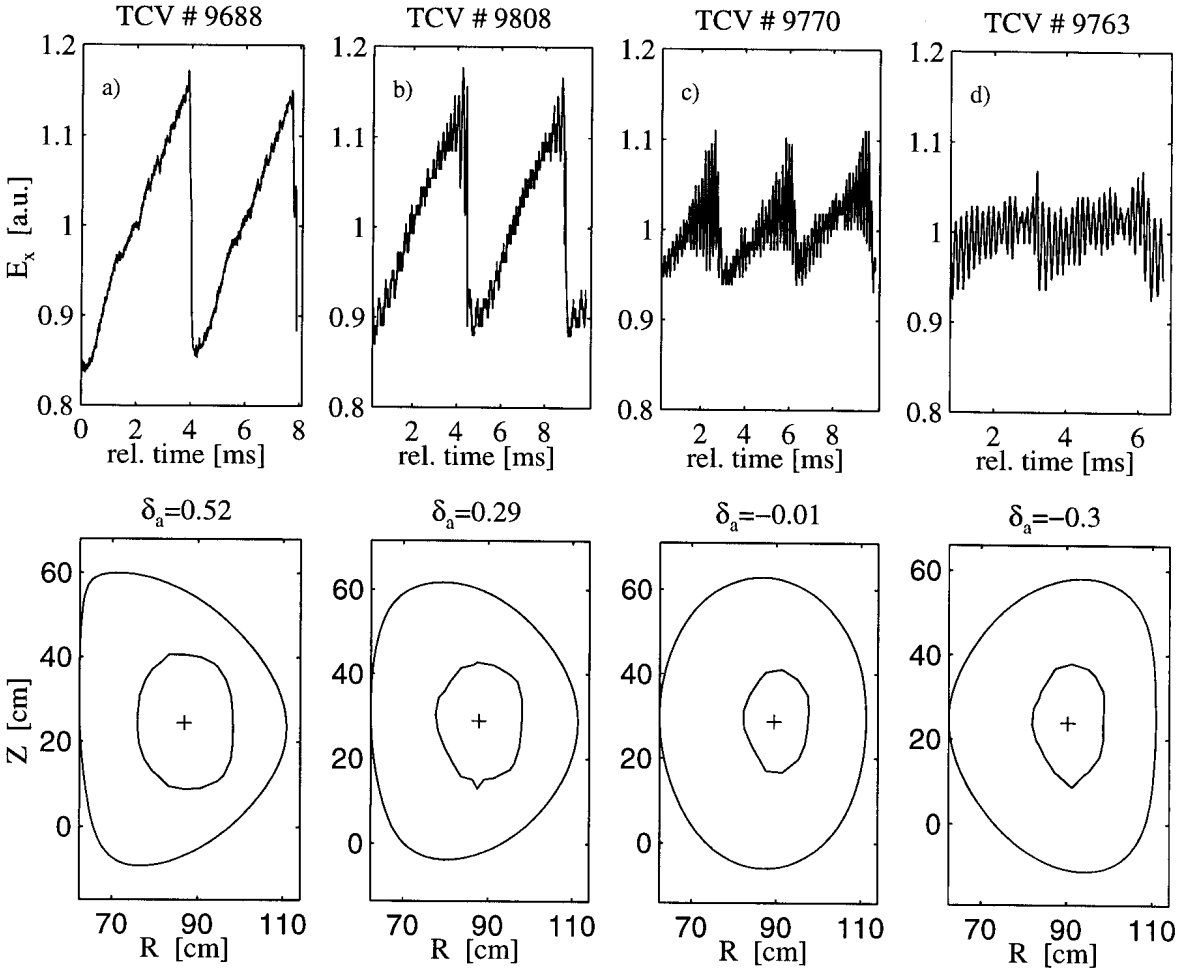

Fig. 4 Sawtooth inversion radius (bottom, inner contours) and LCFS (outer contours) for four different triangularities. Raw X-ray signal with sawtooth and Mirnov oscillations are shown at the top of the figure. All discharges had q_a=3.5, $\bar{n}_e$ =5.0·10^{19}m^{-3}, κ_a=1.4.

The reduction in sawtooth inversion radius only partly explains the reduced sawtooth amplitudes. The normalized sawtooth inversion radius, defined here as $\rho_{inv}=(A_{inv}/A)^{1/2}$, where A_{inv} is the poloidal cross sectional area within the inversion contour and A the plasma cross sectional area within the LCFS, depends essentially only on the cross sectional area averaged current density $\langle j\rangle=I_p/A$. This is shown in figure 5a, for all data for which tomographic reconstructions could be obtained. For the abscissa we use the non-dimensional current density $\langle j\rangle^*=\mu_0 R_0\langle j\rangle/B_T$. A value of $\langle j\rangle^*=1$ corresponds approximately to a safety factor q_{95}=2.5 and for nominal TCV conditions, to $\langle j\rangle$=1.25MA/m^2. The symbols refer to classes of δ_a, showing that there is no intrinsic dependence of $\rho_{inv}\sim\langle j\rangle^*/2$ on δ_a. In a triangularity scan at constant

value of q_a, as performed in these experiments, <j>, and hence ρ_{inv} decrease as δ_a is reduced. However even when <j> and hence ρ_{inv} are fixed, sawtooth amplitudes still exhibit a strong dependence on triangularity as shown in figure 5b. The sawtooth period is slightly shorter for $\delta_\alpha<0$ (typically 4ms) than for $\delta_\alpha>0$ (typically 6ms). This difference is however too small to explain the variation in amplitude by a difference in the duration of the post-crash reheat phase.

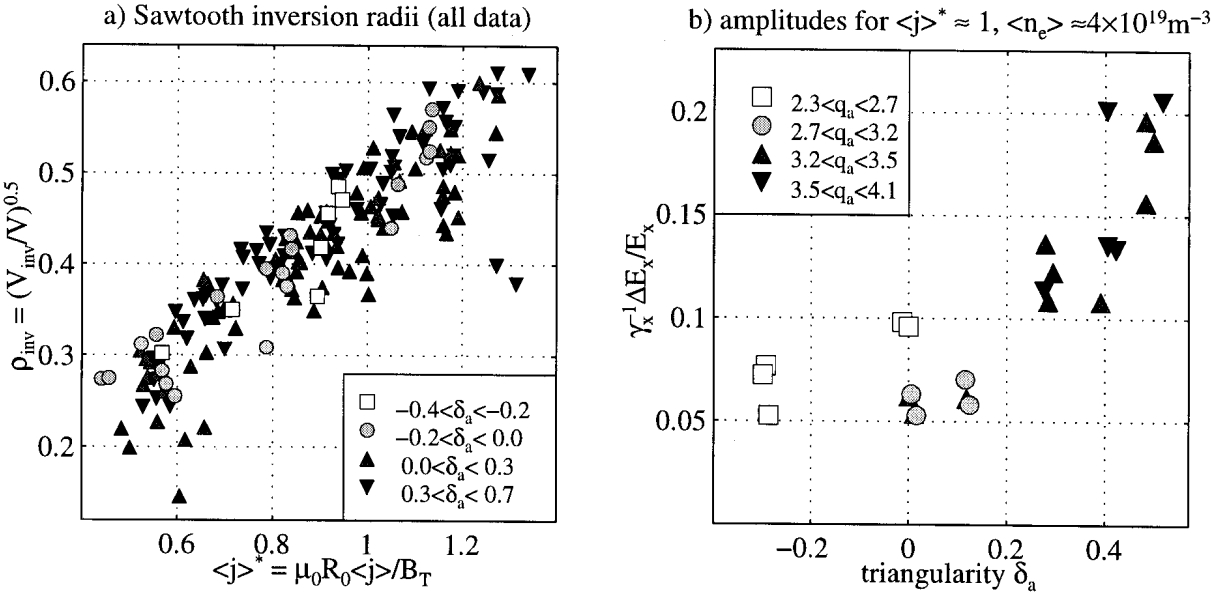

Fig. 5 *a) Sawtooth inversion radius versus non-dimensional average current density. b) Sawtooth amplitudes for fixed values of average current and electron density versus triangularity.*

The sawtoothing behaviour with triangularity raises the question of whether the high sawtooth amplitudes at high positive triangularity may be responsible for confinement deterioration. Temperature profiles in ohmic TCV discharges are essentially trapezoidal in shape, with a central flat section delimited by the inversion radius. Sawtoothing prevents the establishment of temperature gradients in the core. If we assume that in the absence of sawteeth the same gradient as obtained outside the inversion radius could be established inside, we may associate sawtoothing with a deficit ΔW_s of stored energy. The relative deficit $\Delta W_s/W$ is approximately equal to ρ_{inv}^3 and hence smaller than 25% even for the largest inversion radii observed. The sawtooth deficit is therefore not sufficient to explain the large dependence of confinement on triangularity seen in figure 2.

The loss of the sawtooth at negative triangularity often coincides with the onset of MHD activity, which hampers operation by increasing the likelihood of locked mode disruptions at

negative triangularity and sometimes causes confinement deterioration. Mirnov oscillations are typically only present as brief precursor or postcursor oscillations in discharges with high positive triangularity. As the triangularity is reduced the duration of these oscillations increases until they become continuous at negative triangularity, regardless of sawtooth phase (figure 4). The oscillations have been identified to have an n=1 structure from toroidally spaced X-ray measurements [Furno et al 1997]. The dominant mode as identified from SVD on tomographic reconstruction is usually localized on the sawtooth inversion radius and has an m=1 structure. Poloidal structures with m=2 and m=3 are also identified at high mode amplitudes and are sometimes dominant.

1.3 Radiation losses

Changes in plasma radiated power cannot explain the changes in confinement. Figure 6 shows the total radiated power P_{rad} from multi-channel bolometry as a function of ohmic input power. Symbols refer to classes of confinement time. The radiated fraction $f_{rad}=P_{rad}/P_{oh}$ ranges from 20 to 50% and is highest for those conditions which have the best confinement. The higher radiated fraction in discharges with better confinement can be related to the reduced ohmic input power which is necessary to sustain those discharges.

No intrinsic dependence of the radiated power fraction on triangularity has been observed. Instead, f_{rad} decreases as the edge electron temperature increases (figure 7a) with increasing values of input power per particle in the discharge P_{oh}/N_e, where $N_e = \int n_e dV$ is the volume integrated electron density (figure 7b). Only discharges with low elongation ($\kappa<1.2$) appear to have a slightly lower radiated fraction for a given value of $T_e(0.9a)$. Most of the radiated power within the LCFS is due to emission from H- and He-like carbon and to a lesser extend, boron. This has been determined from spectroscopic measurements in the ultra-soft X-ray range (200-800 eV) and modelling of the ionization equilibrium and the radiation using the IONEQ code [Weisen et al, 1996]. The modelling shows that the majority of the emission originates from the plasma periphery, typically outside r=0.7a. The radiated fraction decreases as the edge temperature rises because the fraction of the He- and H-like light impurities, which contribute most of the radiated power, decrease with temperature. The localisation of most of the radiation near the edge is confirmed by bolometric tomography which also shows a poloidally asymetric emission maximum at the inner wall limiting area. The plasma impurity content also is strongly correlated with P_{oh}/N_e. Both X-ray and visible Bremsstrahlung measurements

indicate that Z_{eff} increases from values near 1.5 to near 4 as P_{oh}/N_e is increased from $0.4 \cdot 10^{-14}$ to $2 \cdot 10^{-14} Wm^3$. Discharges with negative triangularity have a somewhat higher impurity content, possibly owing to a smaller plasma-wall interaction area and higher local heat flux on the inner wall.

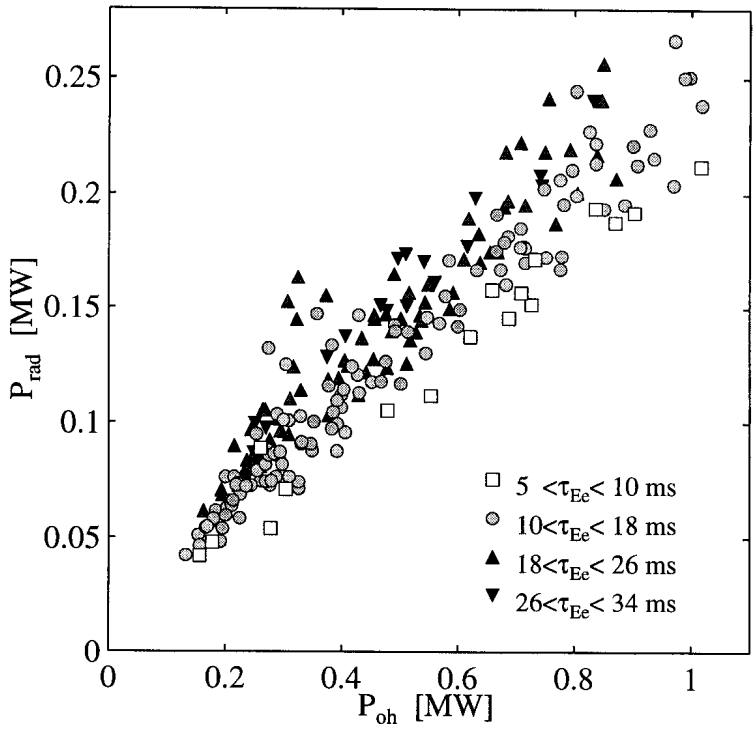

Fig. 6 Radiated power versus ohmic input power. Symbols refer to classes of electron confinement time.

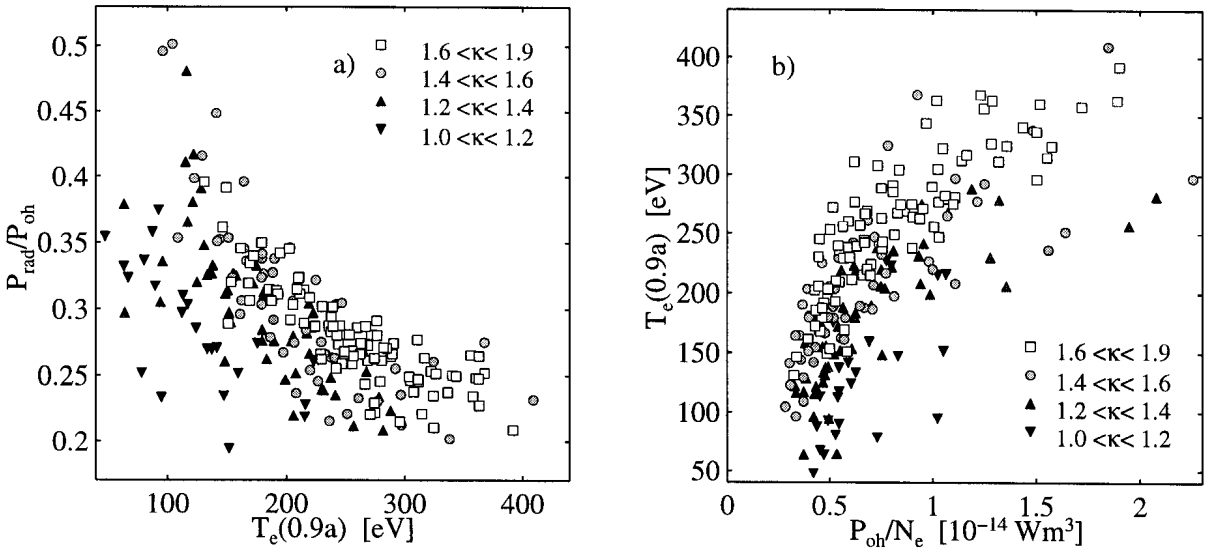

Fig. 7 a) Radiated power fraction versus boundary electron temperature at r/a=0.9. The different symbols refer to classes of elongation. b) Boundary electron temperature versus power per electron.

2.0 Transport analysis

2.1 Local power balance

In figure 8 the flux surface averaged ohmic heat q_{oh} flux is plotted versus the electron temperature gradient for the gradient region ($0.7<r/a<0.9$) for all shapes and all plasma currents but at fixed local density, $n_e(0.8a)\approx 4\cdot 10^{19} m^{-3}$. The radiated power, which is a small correction, has been neglected. The effect of power degradation is clearly apparent. No systematic influence of of the triangularity (figure 8b) on the relationship between heat flux and temperature gradient is observed. Some discharges at high elongation do hovewer sustain somewhat larger gradients for a given heat flux (figure 8a).

Since the electron and ion loss channels cannot be separated for lack of an adequate ion temperature profile measurement, the ratio $q_{oh}/(n_e\langle\nabla T_e\rangle)$ in figure 8 can be viewed as an effective heat diffusivity defined as $\chi_{eff} = \chi_e + \chi_i((n_i\nabla T_i)/(n_e\nabla T_e))$.

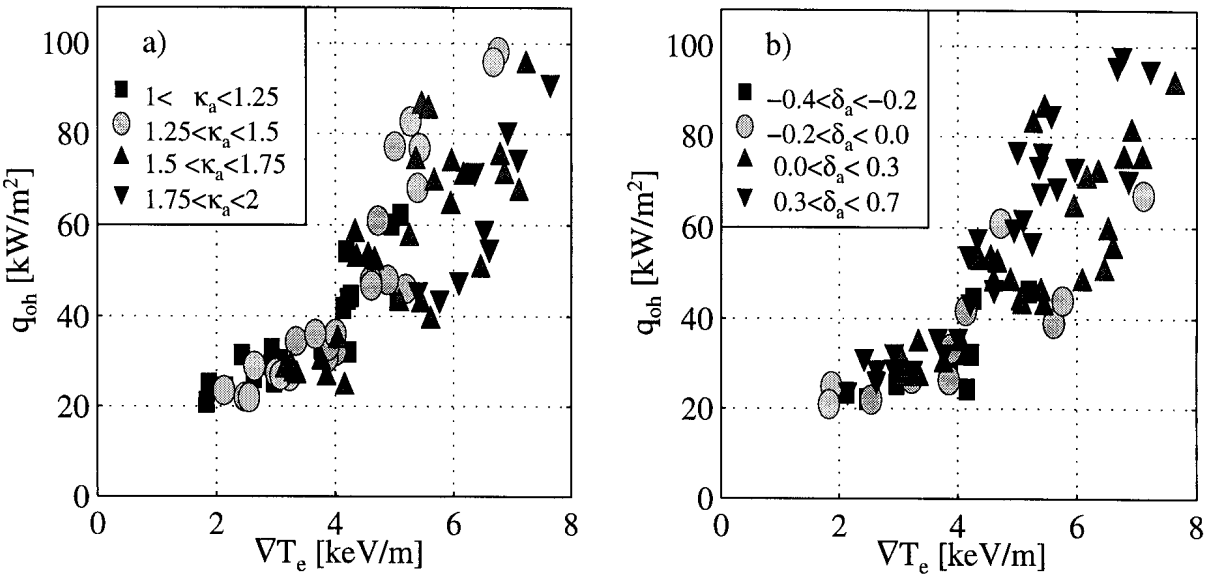

Fig. 8 Plot of the heat flux versus the temperature gradient in the region $0.7<r/a<0.9$ for all shapes and plasma currents for $3\times10^{19}\ m^{-3}<\bar{n}_e(0.8a)<5\times10^{19}\ m^{-3}$. Symbols represent classes of elongation (left) and of triangularity (right).

2.2 Geometrical effect of plasma shaping

The measurements and discussions in the previous sections have ruled out sawtoothing, radiation losses and changes in transport parameters as causes for the large variations in confinement time with plasma shape. The only remaining explanation must hence be associated with temperature gradient changes due to changes in flux expansion or compression resulting from plasma shaping.

A direct geometrical effect of the shaping is a modification of the flux surface separation and consequently of the gradients of plasma parameters such as the temperature and density. Since the existence of a relationship between fluxes and gradients is an established experimental fact [see e.g Connor 1995 and references therein], shaping will influence the conducted heat flux for a given temperature profile. Conventionally the heat flux is expressed as $q = -\lambda \nabla T$, where $\lambda = n\chi$ is the heat conductivity and χ is the thermal diffusivity. It should however be emphasized before the discussion to follow that a relationship between fluxes and gradients may be, but need not be, due to heat diffusion; that it may be, but need not be, determined by local plasma parameters. Owing to the large thermal conduction along magnetic field lines, the temperatures, *T*, of both the ions and the electrons are assumed constant on a magnetic flux surface. Since the poloidal magnetic flux distribution, ψ, depends not only on shape but also on the current distribution, it is not an appropriate choice to account only for shaping effects. Profiles are therefore mapped onto a real spatial coordinate r, chosen as the distance from the magnetic axis measured at the outer midplane and normalised such that $r = a$ on the last closed flux surface (LCFS). The heat flux may then be written as

$$q = -\lambda (dT/dr)(dr/d\psi)\nabla\Psi \qquad [1]$$

The spatial distribution of the gradient geometrical factor, $(dr/d\psi)\nabla\Psi$, is illustrated in figure 9 for two different shapes corresponding to negative and positive triangularity. The compression of flux surfaces toward the outer tip of a positive triangularity shape creates an extended region with increased gradients. At negative triangularity, this region shrinks due to increased separation of the flux surfaces away from the equatorial plane and a larger volume of the plasma can benefit from locally decreased gradients and hence reduced thermal conduction. The large variation in this gradient geometrical factor requires it to be included in any analysis of the local energy balance.

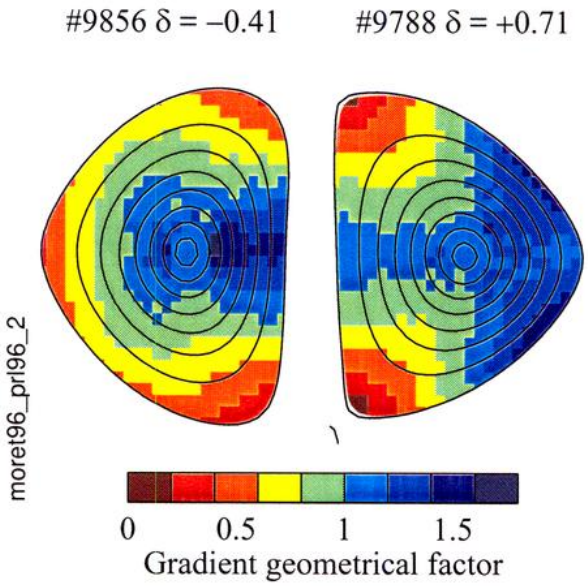

Fig. 9 Spatial distribution of the gradient geometrical factor for a negative and positive triangularity shape. The machine axis is on the left side.

2.2.1 Global shape enhancement factor

The global energy confinement time is a complicated average of the profiles of density, thermal diffusivity, power deposition and geometrical factors. To quantify the influence of geometry alone, the energy confinement time of a shaped plasma can be compared with that of a cylindrical plasma with concentric flux surfaces having the same horizontal width, thermal diffusivity and heat flux, q, associated with the input power deposition profile. Assuming in a first step that the thermal diffusion coefficient depends neither on the poloidal angle nor on the temperature gradient, the temperature profile and the corresponding stored energy can be calculated by integration. It is convenient to define a Shape Enhancement Factor H_s as the ratio of the confinement time to that of the reference cylindrical plasma (indexed 0) with the same value of q/λ and the same density profile:

$$H_s = \frac{S_o \int_0^a \left(\int_r^a \frac{q}{\lambda} \frac{1}{\langle \nabla \Psi \rangle} \frac{d\Psi}{dr} dr' \right) n dV}{S \int_0^a \left(\int_r^a \frac{q}{\lambda} dr' \right) n dV_o} , \qquad [2]$$

where S symbolises the area of the LFCS and n can stand either for the electron or the ion density depending on the context. Since the definition assumes the same heat flux for the reference and test case, the ratio of stored energies in the above expression has been multiplied by the ratio of total powers which is equal to S_0/S. Values of $H_s > 1$ imply an improvement of energy confinement with respect to a circular plasma. The inner integral in expression 2 is a weighted average of $(dr/d\psi)\nabla\Psi$ by the profile of q/λ. This is chosen to be equal to $-dT_0/dr$ where T_o is the normalized temperature profile of the reference plasma. Hence it is not necessary to know the profiles of heat conductivity and heat deposition a priori if a experimental reference discharge is available. For the purpose of the present study we chose T_o to be the average of the normalised temperature profiles, of all plasmas studied (figure 10a). Figure 10b shows the profiles of $(dr/d\psi)\nabla\Psi$ for the two configurations of figure 9. The temperature profiles in the experiments described are approximately trapezoidal with a nearly constant value inside the sawtooth inversion radius, which is characteristic of sawtoothing ohmic discharges. The weighting function is then essentially zero up to mid-radius and nearly constant outside so that gradient geometrical effects are most effective in the outer region of the plasma. We here also assumed a flat density profile for simplicity and universality. Although the density profiles in these experiments are not flat, they are always flatter than the corresponding temperature profiles.

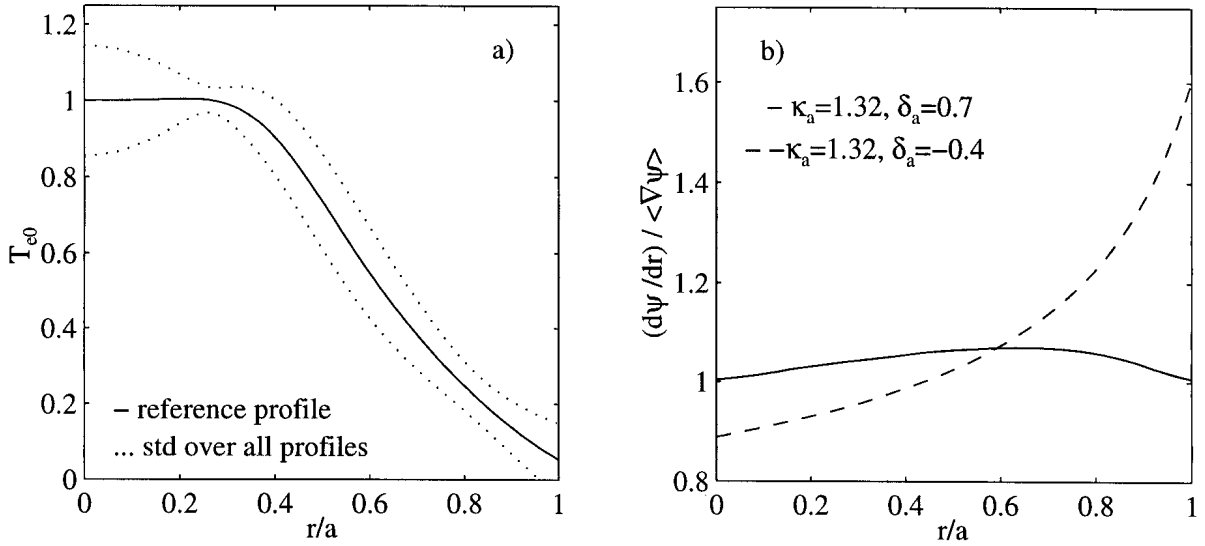

Fig. 10 a) Reference electron temperature profile mapped onto normalized midplane coordinate for TCV shot 9788. The dotted lines show the standard deviation of profiles in these experiments. b) Gradient geometrical factor for shot 9788 (continuous line, κ_a=1.32, δ_a=0.71, q_{95}=5.3, H_s=1.25) and shot 9856 (broken line, κ_a=1.32, δ_a=-0.41, q_{95}=5.1, H_s=1.45).

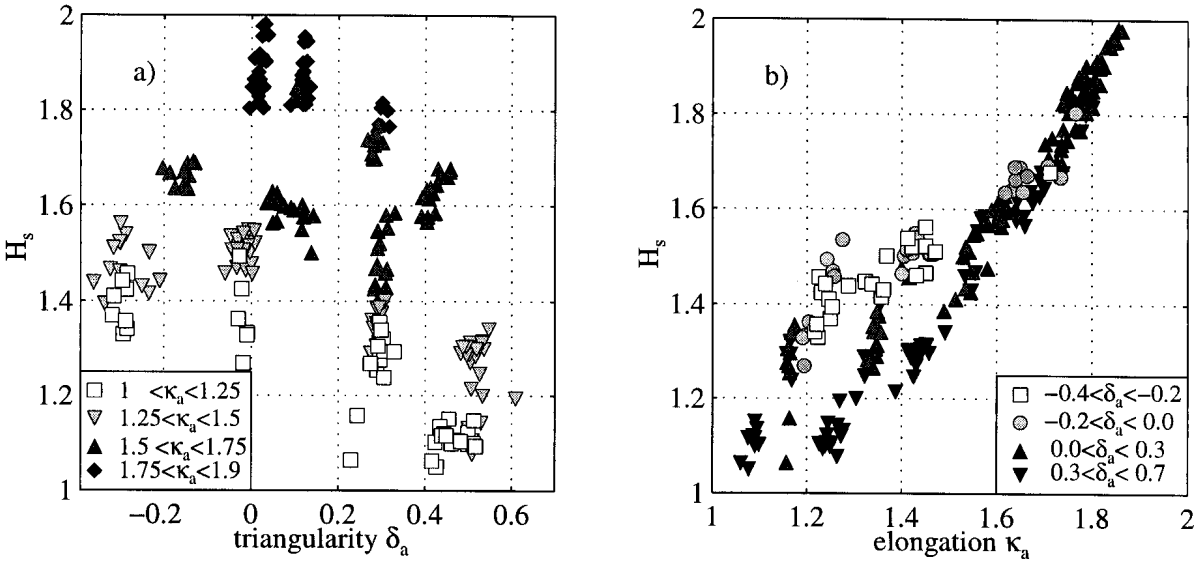

Fig. 11 Shape Enhancement Factor H_s versus triangularity (a) and versus elongation (b).

In figure 11 we show H_s for the whole range of discharges which were created. H_s increases with increasing elongation and decreasing triangularity. For fixed triangularity $0.2<\delta_a<0.3$, H_s is essentially equal to κ_a in the range investigated.

2.2.2 Effect of poloidal variations on shape enhancement factor.

In the above definition of H_s we neglected the possibility of a poloidal variation of heat conductivity. Since there is a clear temperature gradient dependence (figure 6), a poloidal dependence of λ may result from the variation of ∇T along a poloidal flux contour. The error which may be caused by neglecting the poloidal dependence can be estimated assuming a linear dependence of the form $\lambda = \lambda_0 + \lambda_1 \nabla T$, resulting in an effective thermal conductivity, $\lambda_{eff} = -\langle q \rangle / \langle \nabla T \rangle = \lambda_0 + \lambda_1 \langle \nabla T \rangle (\langle (\nabla \psi)^2 \rangle / \langle \nabla \psi \rangle^2)$. The geometrical factor, $\langle (\nabla \psi)^2 \rangle / \langle \nabla \psi \rangle^2$ for the configurations studied lies between 1.01 and 1.065. This implies that a local dependence of the thermal diffusivity on ∇T cannot (and need not) be distinguished from an identical dependence on $\langle \nabla T \rangle$.

If, as before, a dependence of the thermal conductivity on either ∇T or $\langle \nabla T \rangle$ is introduced but now restricted to constant λ_1/λ_0, for trapezoidal profiles of T_o, the derived temperature profile has the same shape multiplied by a numerical factor. This factor is unity for small

energy flux and behaves asymptotically like $q^{-0.5}$. In addition and more importantly, it has no geometry dependence and cancels out in the definition of H_s. Thus, the above defined H_s can still be retained to account for gradient geometrical effects on the energy confinement time in the presence of a temperature gradient dependent thermal conductivity or heat flux degradation.

2.2.3 Energy confinement times corrected for shape effects

Since power degradation is already apparent in the local power balance (figure 8), we should not expect H_s alone to explain the shape dependence of the confinement time. Correction of the measured confinement times using a correction factor equal to H_s only results in partial cancellation of the shape dependence (Moret et al. 1996).

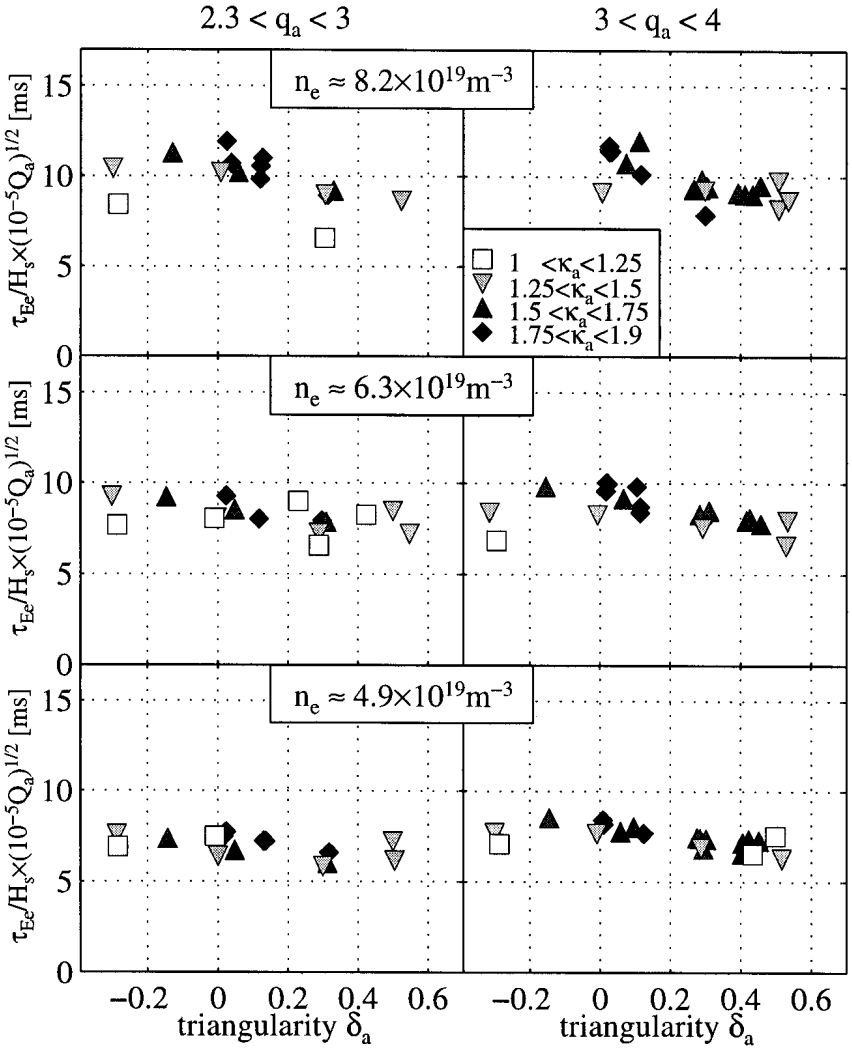

Fig. 12 Electron energy confinement time corrected for the shape enhancement factor and power degradation for three classes of electron density and two classes of safety factor.

Since the shape enhancement factor is defined for a given heat flux (to order zero), the effect of power degradation has to be included a posteriori in order to account for the order-of-magnitude variation of $Q_{oh}=P_{oh}/S$ over the present dataset. This can be done by assuming an empirical power law dependence of the form $\tau_{Ee} \propto H_s \cdot Q_{oh}^{-\alpha}$. In figure 12 we see that correcting the electron energy confinement time by a factor proportional to $H_s \cdot Q_{oh}^{-\alpha}$, with $\alpha=1/2$, results in cancelling most of the shape dependence. The small residual dependence is due to the assumption of a single normalized reference profile T_{e0}, the neglect of the density profile in the calculation of H_s, and possibly to power degradation being different from the power law assumed.

Instead of assuming a single reference profile for T_e and n_e in the definition of H_s (eq. 2) we can obtain an improved description of the effect of shape by using the profiles of temperature and density measured for each discharge [Franke 1997]. In this approach H_s is used as an interpretive tool rather than, as above, predictively. Alternatively a refined predictive H_s can be obtained by making use of the observed relation between profile peaking and average current density in these ohmic discharges (see section 3.2).

3.0 Ohmic profile behaviour and response to confinement changes

The combined effect of shaping, density dependence and power degradation lead to a variation of the confinement time of more than a factor of 4 for range of parameters studied in these experiments. Confinement determines the power required to sustain a chosen ohmic plasma current and hence indirectly influences discharge behaviour.

3.1 Effect of confinement on temperature and ohmic power

The effect of a change of plasma confinement on plasma parameters can be understood from the expression of ohmic heating power,

$$P_{oh}= I_p V_l = <\sigma> V_l^2 A/(2\pi R), \qquad [3]$$

together with the definition for the electron confinement time,

$$P_{oh}= 1.5\ e\ V <n_e T_e>/\tau_e, \qquad [4]$$

where V_l is the loop voltage at the last closed flux surface, $<\sigma>$ is the cross-section averaged electrical conductivity, A the cross sectional area, R the major radius, V the plasma volume, $p_e = 1.5en_eT_e$ the volume averaged electron thermal energy (with T_e in eV) and τ_e the electron confinement time. We introduce normalized profiles, denoted by an asterisk, such as $p_e^* = p_e/p_e(0)$, and profile form factors defined as the volume (or area, as applicable) averages of the normalized profiles, such $<p_e^*>_V$ and $<\sigma^*>_A$, describing the width of the profiles. Assuming Spitzer conductivity, $\sigma = c_\sigma T_e^{3/2}$, where $c_\sigma = 9.7\cdot10^3 Z_{eff}[0.29+0.46/(1.08+Z_{eff})]/\ln\Lambda$ [Soltwisch et al 1984], we can solve equations [3] and [4] for $T_e(0)$ and P_{oh}:

$$T_e(0) = \left\{ \frac{2j^2(0)}{3ec_\sigma} \cdot \frac{2\pi AR}{V} \cdot \frac{\langle p_e^* \rangle}{\langle \sigma^* \rangle} \cdot \frac{\tau_e}{n_e(0)} \right\}^{2/5} \qquad [5]$$

$$P_{oh} = \left[\frac{27e^3}{8c_\sigma^2}\right]^{1/5} \cdot \left[\frac{2\pi R}{A}\right]^{2/5} \cdot V^{3/5} \cdot \frac{\langle p_e^* \rangle^{3/5}}{\langle \sigma^* \rangle^{2/5}} \cdot I_p^{4/5} \cdot \left[\frac{n_e(0)}{\tau_e}\right]^{3/5} \qquad [6]$$

Equations [5] and [6] provide a good description of the data as seen in figure 13, comparing the measured values of $T_e(0)$ and V_l to those expected. The central current density j(0) was taken to be equal to $I_p/(<\sigma^*>A)$ and $<\sigma^*> = <(T_e^{3/2})^*>$ consistently with the assumption of Spitzer resistivity. Equations [5] and [6] show that an ohmic plasma will respond to a change in confinement time mainly by reducing the power necessary to sustain the chosen current ($P_{oh} \sim \tau_e^{-3/5}$) and a more modest increase in temperature ($T_e \sim \tau_e^{2/5}$).

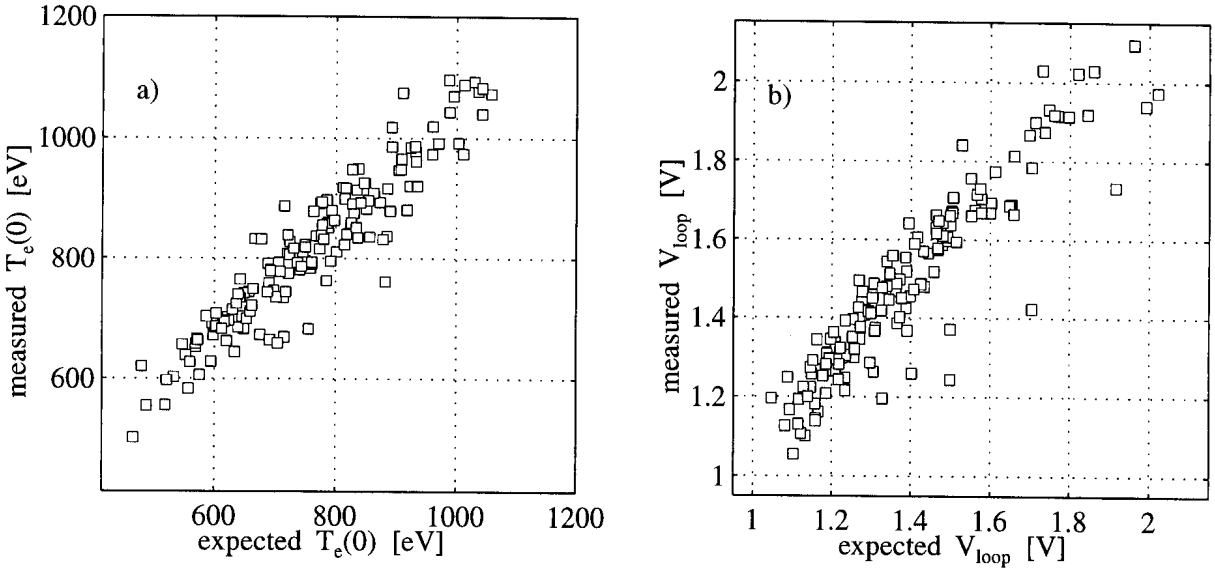

Fig. 13 a) Measured central electron temperature versus central temperature expected from ohmic response (eq.3). b) Measured loop voltage versus loop voltage expected from ohmic response (eq. 4).

3.2 Profile effects

Additional dependencies in equations 5 and 6 can arise from the ratios of form factors. In all discharges investigated we however found that $\langle\sigma^*\rangle \approx \langle p_e^*\rangle$, effectively removing the form factor dependencies (figure 14a). The form factors scale linearly with current density (figure 14b), with $\langle\sigma^*\rangle \cong 0.4\langle j\rangle^*$, where $\langle j\rangle^* = \mu_0 R_0 \langle j\rangle / B_T$ is a non-dimensional current density. This relation would imply $q(0) \approx 0.85$ if the Spitzer conductivity profile were strictly proportional to the current profile. These intriguing observations, although not central to the subjects developed in this article, is reminiscent of reports on electron temperature or pressure profile 'consistency' or 'resilience' reported from several experiments [Coppi 1980, Goldston et al 1986, Taroni and Tibone 1986, Gruber et al 1987]. The relationships seen in figures 14 a and b are consistent with Kadomtsev's [1987] and Biskamps [1986] predictions based on the idea of plasma self-organization to a state of minimum energy. Alternatively the observed relationship $\langle\sigma^*\rangle \cong 0.4\langle j\rangle^*$ may be interpreted as due to relaxation of the current profile to a state of maximum entropy [Minardi and Lampis 1990]. In that view the relation $\langle\sigma^*\rangle = \langle j\rangle^* = \langle p_e^*\rangle$ would have to follow from the plasma equilibrium force balance [Minardi 1997].

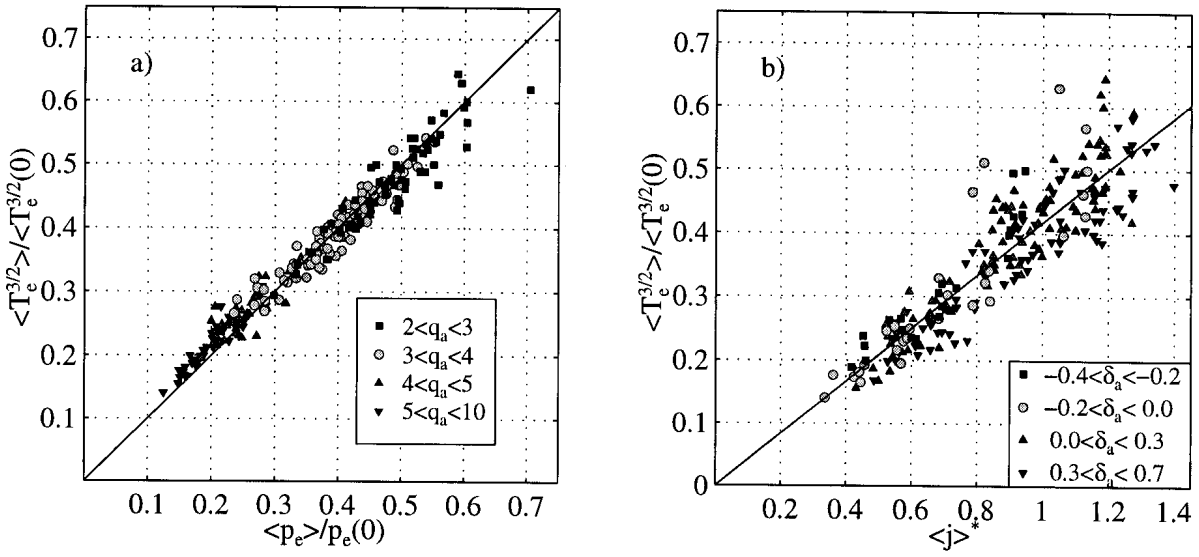

Fig. 14 a) Relation between profile form factors for plasma pressure and plasma conductivity. Symbols refer to edge safety factor. b). Peaking of conductivity profile versus normalized current density $<j>^* = \mu_0 R_0 <j>/B_T$. *Symbols refer to classes of triangularity.*

3.3 Combined effect of confinement changes and power degradation in ohmic plasmas

The confinement time depends itself on heat flux through the effect of power degradation, which can be expressed by an empirical relation such as

$$\tau_e = \tau_{e0}(Q/Q_0)^{-\alpha} \qquad [7]$$

where Q is the heat flux through the last closed flux surface, Q_0 refers to a reference case, and τ_{e0} is an underlying confinement time. The effect of power degradation amplifies any underlying changes of confinement in ohmic plasmas, as seen when combining eq.5 with the lead dependencies in eqs. 5 and 6:

$$\tau_e = \tau_{e0}^{\gamma} \text{ where } \gamma = 1/(1-5\alpha/3). \qquad [8]$$

For α=0.5, which is typical for most tokamak experiments, γ is equal to 10/7. Figure 15 (squares) shows this effect for a class of discharges with fixed average electron and current densities, but with a wide range of shape enhancement factors $H_s \sim \tau_{e0}$. When the confinement times are corrected only for H_s compensation of the shape dependence is incomplete (circles). It is complete only when a correction factor equal to $H_s^{10/7}$ is used, consistently with eq. 8 (triangles).

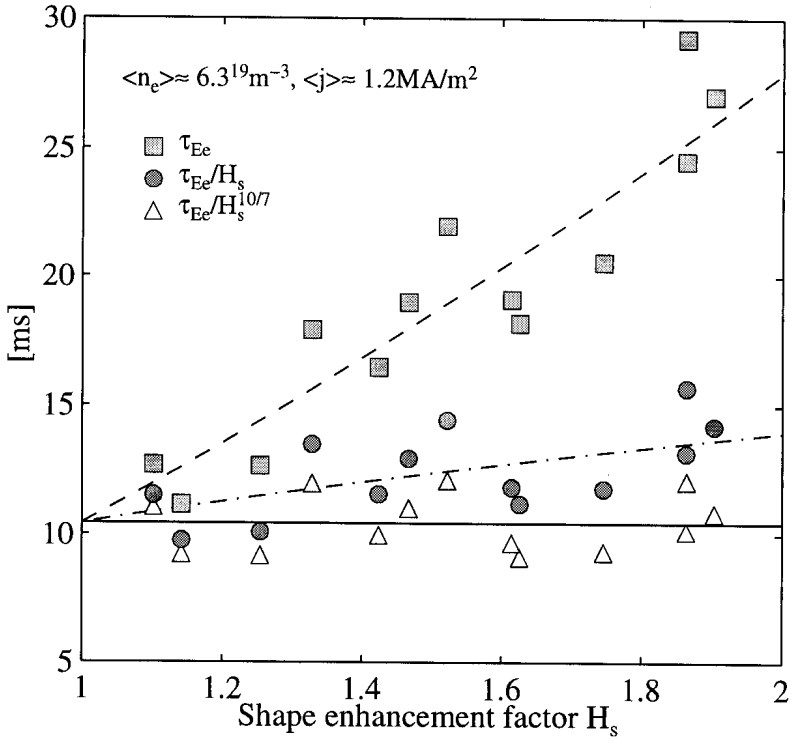

Fig. 15 Confinement time versus H_s for $\bar{n}_e = 6.3 \cdot 10^{19} m^{-3}$ and <j> = 1.2 MA/m^3. Squares: Measured electron confinement times τ_{eE}. Circles: Confinement time τ_{eE}/H_s corrected for shape only. Triangles: Confinement time $\tau_{eE}/H_s^{10/7}$ corrected for shape and power degradation.

Hence the range of H_s, which spans a range of a factor of 2, translates into a range of confinement times spanning a factor of 2.7. The observation that for fixed electron and current densities, confinement time depends only on H_s^{γ} suggest that these two quantities, or closely related quantities, may be fundamental to ohmic confinement (see section 5). The confinement changes seen in the shape scans at fixed safety factor and electron density can be considered as resulting from the combined effects of changes in H_s, current density changes, and power degradation.

4.0 Effect of confinement on sawtoothing and MHD activity

The sawtooth reheat rate reflects the electron power balance in the plasma core during the sawtooth ramp phase:

$$\frac{dw_e}{dt} = p_{in} - p_{ei} - p_{rad} - \mathrm{div}(q_c) \qquad [9]$$

where p_{in} is the ohmic input power density, p_{ei} is the electron-ion equipartition, p_{rad} is the radiated power density and q_c represents losses due to conduction and convection. An estimate of dw_e/dt has been obtained from the time evolution of the tomographically reconstructed local soft X-ray emissivity E_x.

$$\frac{dw_e}{dt} \cong \frac{3e\langle n_e T_e\rangle_t dE_x}{2\gamma_x E_x dt} \qquad [10]$$

where $\gamma_x = d(\ln E_x)/d(\ln T_e(0))$ was taken as the logarithmic derivative of the temperature dependence of the main radiating impurity, carbon. The time average electron density and temperatures were obtained from low time resolution (50ms) Thomson scattering measurements. Besides reconstruction errors, uncertainties in this estimate stem from the possible presence of other impurities and from the assumption that the pressure increase is due to an increase in temperature only. Figure 16 shows the core reheat power density averaged over the tomographically determined inversion radius, versus the ohmic heating power density, also averaged over the inversion radius and estimated under the assumption that the current profile is proportional to the $T_e^{1.5}$ profile. The figure has been restricted to a range of electron densities near $6.3 \cdot 10^{19} m^{-3}$. The figure shows that the reheat power is comparable to the ohmic heating power. The difference, typically $0.3 MW/m^3$, can be attributed to the losses in above balance equation. The total radiation inferred from the observed x-ray radiation was determined to be only a few tens of kW/m^3. Also, in the absence of strong mode activity, conduction and convection losses are unlikely to be important in the flattened core region of the discharge. We conclude that the observed difference between ohmic input power and reheat power is mostly due to electron-ion equipartition.

The observation in figure 3 can now be understood from core power balance considerations. Any reduction in ohmic input power will also lead to a reduction of sawtooth reheat power. Reductions in ohmic input power may be caused by current density reductions (operation at high q_{95}) or by improvement in energy confinement as discussed in section 4.1 and 4.3. In figure 16 we see that the plasmas with the highest confinement times tend to have lower ohmic heating powers and hence lower sawtooth reheat powers and smallest amplitudes ($\Delta w_e = \Delta t_{saw} dw_e/dt$). The shorter sawtooth periods for $\delta<0$ (~4ms) than for $\delta>0$ (~6ms) also contribute to the smaller sawtooth amplitudes at negative triangularity. Ironically the variations

in sawtooth amplitude with triangularity now appear as side effects of the changes in current density and confinement resulting from plasma shaping, rather, as might appear at first sight, causing the confinement changes.

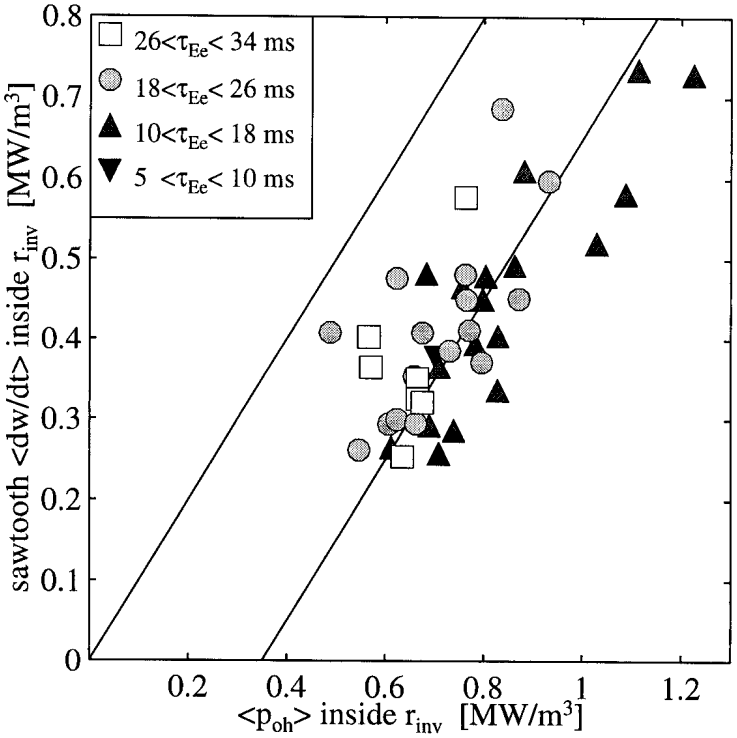

Fig. 16 Sawtooth reheat power versus central ohmic heating power inside inversion radius for $\bar{n}_e=6.3\cdot10^{19}m^{-3}$. *The symbols refer to classes of electron confinement time. The upper line corresponds to* $<dw_o/dt>_{inv}=<p_{oh}>_{inv}$, *the lower line to* $<dw_o/dt>_{inv}=<p_{oh}>_{inv}$- *0.35 MW/m*^{3}.

The increase of mode activity at reduced triangularity may, at least in part, also be attributed to a reduction in ohmic heating power. They also correspond to more peaked temperature profiles which also may contribute to destabilizing resistive modes. This is shown in figure 17 where the relative mode oscillation amplitude from a line integrated X-ray measurement, corrected for the temperature dependence in the same way as used for the sawtooth amplitudes, is plotted versus loss power per electron. As already noted in figure 7 the electron temperature in the boundary region, measured at r/a=0.9 increases with P_{oh}/N_e from near 100 eV to near 350 eV over the range of the abscissa in figure 17. The symbols refer to classes of triangularity. In the majority of cases mode amplitude correlates well with P_{oh}/N_e and boundary temperature. High amplitude modes are unlikely to develop with Te(0.9a) > 200 eV, but are quite frequent at

lower temperatures.

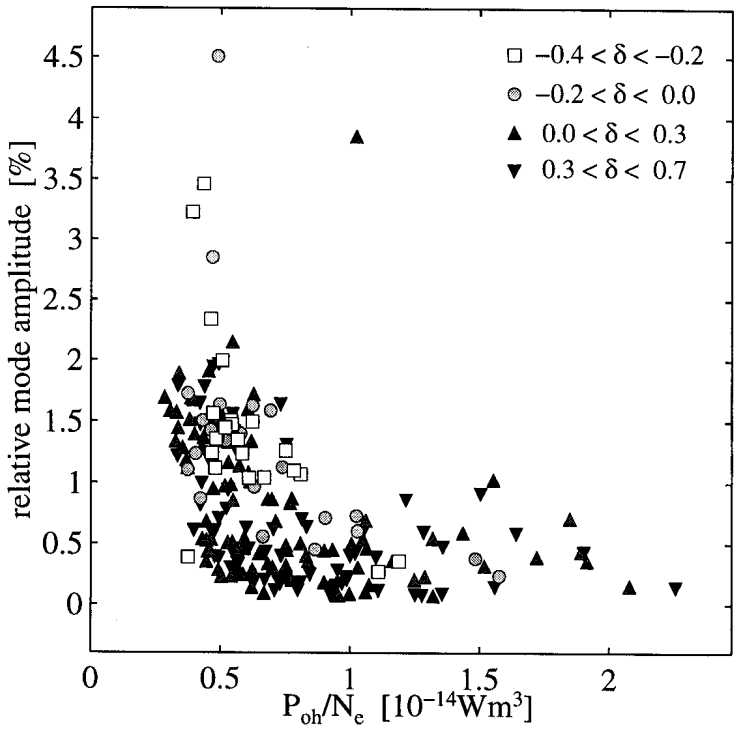

Fig. 17 X-ray mode amplitude versus power per electron. Symbols refer to classes of triangularity.

A similar correlation is observed with the width of the Spitzer conductivity profile $<(T_e^{3/2})>/T_e(0)^{3/2}$, the occurrence of strong modes being more likely with peaked profiles. There is however no correlation of mode amplitudes with central electron temperatures. This observation suggests that the modes correspond to resistive instabilities near the plasma edge. The m=1, n=1 modes observed by X-ray tomography may be produced by toroidal and shape-induced coupling by unstable m>1, n=1 in the colder plasma near the last closed flux surface. Although in most cases the correlation of mode amplitude and P_{oh}/N_e or $T_e(0.9a)$ is good, there are a few notable exceptions (figure 17), corresponding to the highest mode amplitudes, of which most are observed at $\delta<0$. These cases may indicate an intrinsic dependence of resistive mode stability on triangularity. Since the observed amplitudes are not a direct measure of growth rate, the differences may however only reflect shape dependent differences in saturated mode amplitude. Possible intrinsic effects of shape could include differences in shape induced mode coupling and the simple fact that plasmas with high edge flux expansion, such as obtained with negative triangularity, have a relatively larger volume of cold peripheral plasma than plasmas with low edge flux expansion, and may therefore be more prone to developing resistive modes.

5.0 Global scalings using the shape enhancement factor

A promising feature of the shape enhancement factor as presented in section 3.2 is that it may be able to replace geometrical factor in global scaling expressions. We have tested this assertion on two well known scaling expressions for the experimental database presented in this paper. The first of these is the well known Neo-Alcator scaling law for ohmic plasmas. Rather than using the original form of this law [Parker et al. 1986], we use a modified form [Uckan N.A. and ITER Physics Group 1990], which provides a better description of TCV data at fixed plasma shape:

$$\tau_{NA} = 0.07 \times 10^{-20} \langle n_e \rangle a R_0^2 q^* \ , \qquad [11]$$

where $q^* = \frac{5}{2} \cdot \frac{a^2 B_T}{R_0 I_p} \cdot [1 + \kappa^2 (1 + 2\delta^2 - 1.2\delta^3)]$ is a cylindrical equivalent safety factor and $\langle n_e \rangle$ is the volume averaged electron density. In figure 18a we plot the total energy confinement time from our entire dataset against the modified Neo-Alcator scaling law. Since this scaling refers to the total stored energy the ion contribution was estimated as $W_i = W_e n_i T_i(0)/(n_e T_e(0))$ where $n_e/n_i = 1 - (Z_{eff} - 1)/z$ and $z = 6$ consistently with carbon being the main impurity. Z_{eff} was obtained from the core x-ray emissivity and from line-averaged visible Bremsstrahlung measurements. The ion temperature was obtained for low densities from the spectrum of charge exchange neutrals measured using a neutral particle analyser. At medium to high densities the transparency of the plasma to neutrals is insufficient for a measurement of the core ion temperature and NPA measurements lead to an underestimate of $T_i(0)$. Therefore a second lower bound to $T_i(0)$ was obtained by assuming that up 40% of the available ohmic core power density was transferred to the ions by equipartition. The resulting ion contribution to the total energy confinement time rises from near 25% for $\bar{n}_e \sim 3 \cdot 10^{19} m^{-3}$ to near 45% at $\bar{n}_e \sim 8 \cdot 10^{19} m^{-3}$. The symbols in figure 18a refer to classes of shape enhancement factor H_s. We see that the Neo-Alcator expression produces a good prediction for H_s=1, but underestimates the confinement at high values of H_s by a factor of 3. Such disagreement is not unexpected since the expression contains no shape scaling. Figure 18b shows that the Neo-Alcator prediction can be improved by introducing the shape enhancement factor:

$$\tau_{NA\text{-}H_s} = 0.07 \times 10^{-20} H_s^{10/7} \langle n_e \rangle a R_0^2 q^* \ , \qquad [12]$$

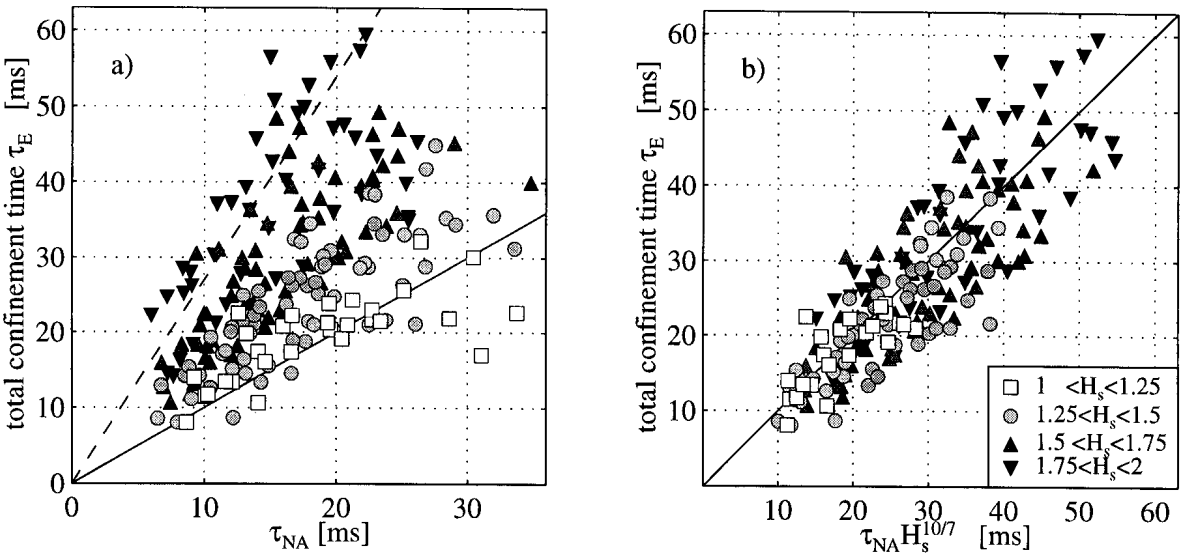

Fig. 18 a) Measured total confinement time versus Neo-Alcator scaling. The lines have slopes equal to 1 and 2.7 respectively. b) Measured confinement time versus Neo-Alcator confinement multiplied by the shape enhancement factor. The symbols refer to classes of shape enhancement factor.

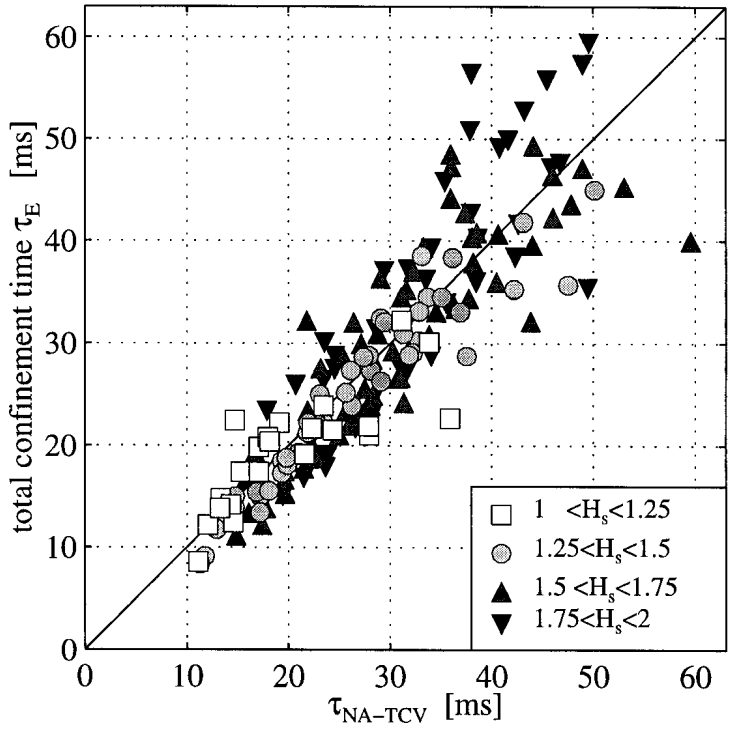

Fig. 19 Measured total confinement time versus Neo-Alcator-TCV scaling expression [eq. 13]. The symbols refer to classes of shape enhancement factor.

where the exponent 10/7 has been introduced to account for power degradation in ohmic plasmas as explained in section 3.3. A further improvement, shown in figure 19 is obtained by fitting the density dependence and by noting that in the presence of large variations of shape $\langle j\rangle^{*}=\mu_0 R_0\langle j\rangle/B_T$ provides a better description than the safety factor:

$$\tau_{NA-TCV} = 0.14 \times a R_0^2 H_s^{10/7} \langle 10^{-20} n_e \rangle^{0.78} / \langle j \rangle^{*} \qquad [13]$$

The comparison of the measured electron confinement time with Rebut-Lallia-Watkins scaling (RLW, Rebut et al 1989, also Uckan and ITER physics group 1989) is shown in figure 20a. The agreement of RLW scaling is remarkable considering the large range of conditions investigated and is largely due to a realistic scaling with elongation ($\tau_{RLW} \sim \kappa^{0.92}$) of the dominant second term in expression 14:

$$\tau_{RLW} = \left\{ 1.2 \times 10^{-2} I L^{1.5} Z_{eff}^{-0.5} + 0.146 \langle n_e/10^{20} \rangle^{0.75} I^{0.5} B_T^{0.5} L^{2.75} Z_{eff}^{0.25} P^{-1} \right\} (A_i/2)^{0.5} \quad , \qquad [14]$$

where $L = (Ra^2\kappa)^{1/3}$, I is the plasma current in MA and P the heating power in MW. The fit can be improved by considering that RLW scaling gives a good description for some fixed value of elongation and by allowing H_s to describe all of the shape dependence. The corresponding scaling expression is given by [15]

$$\tau_{RLW-TCV} = 1.08 \times H_s \left\{ 1.2 \times 10^{-2} I L_0^{1.5} Z_{eff}^{-0.5} + 0.146 \langle n_e/10^{20} \rangle^{0.75} I^{0.5} B_T^{0.5} L_0^{2.75} Z_{eff}^{0.25} P^{-1} \right\} (A_i/2)^{0.5}$$

where $L_0 = (Ra^2)^{1/3}$. The measured confinement time is plotted versus the RLW-TCV scaling and exhibits a further reduction in data dispersion (figure 20b). The significance, if any, of the data points corresponding to some of the highest elongations and electron densities in the dataset and which populate the upper fringe of the distribution is presently under investigation. The numerical coefficient, 1.08, was fitted for the main distribution.

Note that since RLW scaling describes power degradation explicitly the shape enhancement factor is raised to unit power in expression 15. Also both forms of RLW scaling are not predictive for ohmic plasmas since both I and P are used in the scaling expressions. A ohmically predictive form can be obtained however by combining the scaling expression with

equation 6 and eliminating P_{oh}, using the observed relationships between profile parameters $<p^*>$ and $<\sigma^*>$ and the scaling thereof with average current density.

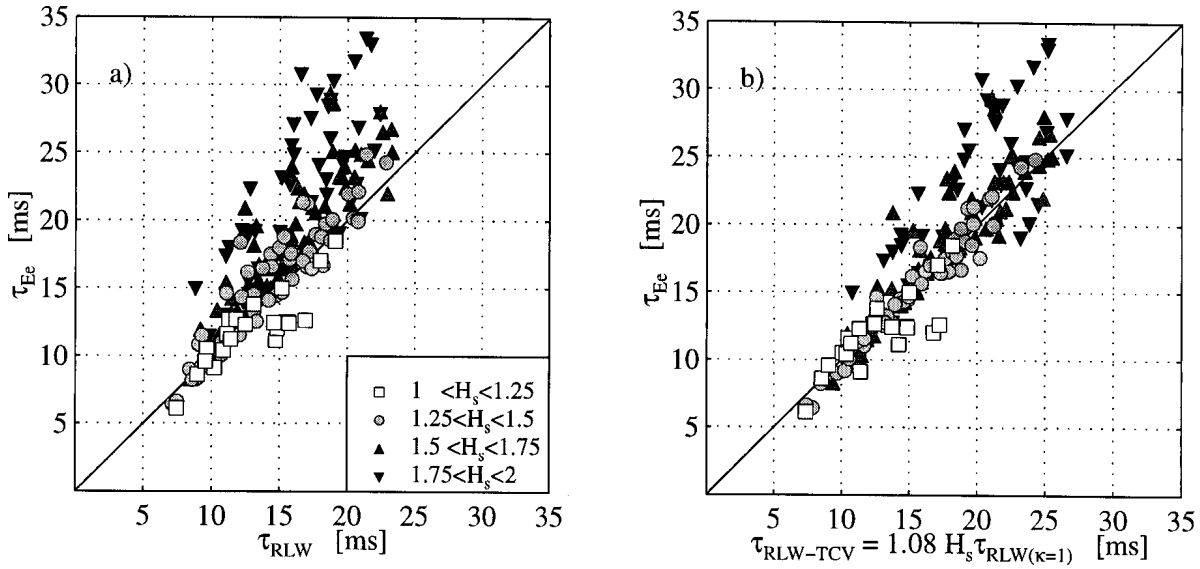

Fig. 20 a) Measured electron energy confinement times versus Rebut-Lallia-Watkins scaling. b) Measured electron energy confinement times versus modified Rebut-Lallia-Watkins scaling (expression 15).

The above examples demonstrate that refined scaling expressions are obtained when expressing the effect of geometry by the single factor H_s. The TCV results also show that confinement scaling with elongation is more favourable than anticipated since $H_s \cong \kappa_a$ for $\delta_a \cong 0.25$.

6.0 Summary and conclusions

Large variations of confinement time have been observed in shaping experiments in limited ohmic L-mode plasmas in TCV. The most unexpected of these is an increase of confinement time as triangularity is reduced to near zero or to negative values. At a constant value of heat flux at the LCFS confinement time scales approximately linearly with elongation in the range investigated (κ<1.9). We have ruled out radiation losses and prompt energy losses due to sawteeth as explanations for these observations. The improvement of confinement time as triangularity is reduced may only apply to discharges at low β since the geometrical shear introduced by triangularity has a stabilizing effect on ballooning modes and ELMs [Hyatt et al. 1994, Itami et al. 1995, JET Team 1995].

Discharges with zero or negative triangularity have smaller sawteeth, higher levels of MHD mode activity and are more likely to disrupt because of locked modes. The lower sawtooth amplitudes can be understood from core power balance considerations and result from a drop in ohmic power $P_{oh} \propto \tau_{Ee}^{-3/5}$ which is consequential to the confinement increase and to the reduction in ohmic current when reducing δ at constant q_a. The increased levels of mode activity may also in part be due to the reduced power necessary to sustain discharges with low or negative triangularity. If this is the case there is scope for suppressing this undesirable effect of negative triangularity by additional heating.

The loop voltage and plasma temperature and density profiles observed in the experiments are consistent with Spitzer resistivity. The profile factors for electron pressure, $\langle n_e T_e \rangle / (n_e(0) T_e(0))$, and Spitzer conductivity, $\langle T_e^{3/2} \rangle / T_e^{3/2}(0)$, are essentially equal in these discharges and in agreement with theoretical predictions based on minimum energy states of the plasma [Biskamp 1986, Kadomtsev 1987]. The profile factors are parametrized by q_{95}, or better $\langle j \rangle^* = \mu_0 R_0 \langle j \rangle / B_T$ with $\langle T_e^{3/2} \rangle / T_e^{3/2}(0) \cong 0.4 \langle j \rangle^*$ irrespective of plasma shape.

The large variation in the measured energy confinement time within the domain of explored equilibria can be explained by direct geometrical effects of shaping combined with heat flux degradation. The effect is successfully described by a shape enhancement factor H_s which is based on a ratio of stored energies of a shaped plasma to that of a cylindrical reference plasma with the same heat flux. The shape enhancement factor depends only on the equilibrium geometry and the profiles of temperature gradient ∇T ($=q/n\chi$) and density, which are assumed to be the same in the reference case and the shaped plasma and can be taken from an experimental measurement. The definition of H_s relies on there being a relationship between heat fluxes and temperature gradients which is conserved as the plasma shape is changed, irrespective of the physics underlying this relationship. Where confinement times changes with shape are not described by H_s, these can be interpreted as being due to changes in the transport coefficients. This may have been the case in some of the discharges with the highest elongation and the highest densities in the experiments described.

The introduction of H_s in the international confinement database has the potential of improving the description of the effect of shape for a given confinement mode and the prediction for ITER by reducing the scatter of which some may result from an inadequate description

of the effect of shape. It remains however to be verified if H_s is as successful for plasmas with auxiliary heating and for different confinement regimes as it is for these limited ohmic L-mode discharges. This work also shows that global confinement can be optimized by appropriate shaping. Negative triangularity and high elongation are not the only options and more general shapes can be envisaged which could result from a compromise between the benefits of the geometry, the possible drawbacks of unfavourable MHD or vertical stability and engineering constraints.

Acknowledgement

The authors wish to thank the entire TCV team for their support. This work was partly funded by the Swiss National Funds for Scientific Research.

References

Anton M, Weisen H, MJ Dutch et al, *Plasma Phys. Control. Fusion* **38** (1996) 1849

Biskamp D, *Comments Plasma Phys. Control. Fusion* **10**, (1986) 165

Connor JW, *Plasma Phys. Control. Fusion* **37** (1995) A119

Coppi B, *Comments Plasma Phys. Contr. Fusion* **5**, (1980) 261

Franke S, *PhD thesis, to be presented at the Department of Physics, Ecole Polytechnique Fédérale de Lausanne, Switzerland* (1997)

Goldston RJ, Frederickson E., McGuire et al, *13th EPS Conference on Contr. Fusion and Plasma Heating*, ECA **10C** part I, 1986, 41

Gruber O, Becker G, Bosch H.S. et al, *14th EPS Conference on Contr. Fusion and Plasma Heating*, ECA **11C** part I, 1986, 45

Furno I, Weisen H, Anton M et al, to be presented at the *24th EPS on Controlled Fusion and Plasma Physics, Berchtesgaden, (D)* 9-13 June 1997.

Hofmann F, Lister J B, Anton M et al, *Plasma Phys. Contr. Fusion* **36**, 1994, B277

F. Hofmann, M.J. Dutch, J.-M. Moret, *Europhysics Conference Abstracts, 22nd EPS Conference on Controlled Fusion and Plasma Physics, Bournemouth*, 1995, edited by B.E. Keen, P.E. Stott and J. Winter, **Vol. 19C**, p. II-101.

Hyatt AW, Lazarus EA, Osborne TH, *21st EPS Conf. on Contr. Fusion and Plasma Physics, Montpellier*, 1994, edited by E. Joffrin, P. Platz and P.E. Stott, ECA **18B**, p. I-14.

Kadomtsev B, *Proc. International Conference on Plasma Physics*, Kiev, 6-12.4 (1987), 1273, edited by A.G. Sitenko, published by World Scientific

Itami K and the JT-60 Team, *Plasma Phys. Contr. Fusion* **37** (1995) A255

JET Team (presented by TTC Jones), *Plasma Phys. Contr. Fusion* **37** (1995) A359

Minardi E and Lampis G, *Plasma Phys. Contr. Fusion* **32** (1990) 819

Minardi E, *personal communication,* February 1997

Moret JM, Franke S, Weisen H et al, *subm. to Phys. Rev. Lett (1986), also CRPP report* LRP 560/96.

Parker RR, Greenwald M, Luckhardt et al., Nuclear Fusion **25**, 1985, p. 1127.

Rebut P H, Lallia P P and Watkins M.L. *JET report* JET_P(88) 05 and corrigendum.

Soltwisch H, Graffmann E, Schlüter J and Waidmann G in *Int. Conf. on Plasma Physics, Lausanne, Switzerland 27.6-3.7 1994, Proc. p 499,* edited by MQ Tran and RJ Verbeck.

Taroni A and Tibone F, *13th EPS Conference on Contr. Fusion and Plasma Heating*, ECA **10C** part I, 1986, 160

Uckan NA and ITER Physics Group, *ITER Physics Design Guidelines: 1989, ITER documentation series, No 10, IAEA, Vienna 1990.*

Weisen H, Piffl V, Weller A *et al., 23rd EPS Conf. on Contr. Fusion and Plasma Phys.*, Kiev, (1996). ECA **20C**, part I, 111.